

# Pronounced Photovoltaic Response from Multilayered Transition-Metal Dichalcogenides PN-Junctions

Shahriar Memaran,<sup>†,‡</sup> Nihar R. Pradhan,<sup>†</sup> Zhengguang Lu,<sup>†,‡</sup> Daniel Rhodes,<sup>†,‡</sup> Jonathan Ludwig,<sup>†,‡</sup> Qiong Zhou,<sup>†,‡</sup> Omotola Ogunsolu,<sup>§</sup> Pulickel M. Ajayan,<sup>||</sup> Dmitry Smirnov,<sup>†</sup> Antonio I. Fernández-Domínguez,<sup>⊥</sup> Francisco J. García-Vidal,<sup>⊥</sup> and Luis Balicas<sup>\*,†</sup>

<sup>†</sup>National High Magnetic Field Lab, Florida State University, 1800 E. Paul Dirac Dr., Tallahassee, Florida 32310, United States

<sup>‡</sup>Department of Physics, Florida State University, Tallahassee, Florida 32306, United States

<sup>§</sup>Department of Chemistry & Biochemistry, Florida State University, Tallahassee, Florida 32306-4390, United States

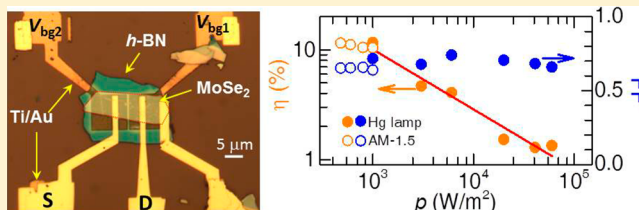
<sup>||</sup>Department of Mechanical Engineering and Materials Science, Rice University, Houston, Texas 77005-1892, United States

<sup>⊥</sup>Departamento de Física Teórica de la Materia Condensada and Condensed Matter Physics Center (IFIMAC), Universidad Autónoma de Madrid, E-28049 Madrid, Spain

## S Supporting Information

**ABSTRACT:** Transition metal dichalcogenides (TMDs) are layered semiconductors with indirect band gaps comparable to Si. These compounds can be grown in large area, while their gap(s) can be tuned by changing their chemical composition or by applying a gate voltage. The experimental evidence collected so far points toward a strong interaction with light, which contrasts with the small photovoltaic efficiencies  $\eta \leq 1\%$  extracted from bulk crystals or exfoliated monolayers. Here, we evaluate the potential of these compounds by studying the photovoltaic response of electrostatically generated PN-junctions composed of approximately 10 atomic layers of MoSe<sub>2</sub> stacked onto the dielectric *h*-BN. In addition to ideal diode-like response, we find that these junctions can yield, under AM-1.5 illumination, photovoltaic efficiencies  $\eta$  exceeding 14%, with fill factors of  $\sim 70\%$ . Given the available strategies for increasing  $\eta$  such as gap tuning, improving the quality of the electrical contacts, or the fabrication of tandem cells, our study suggests a remarkable potential for photovoltaic applications based on TMDs.

**KEYWORDS:** Transition metal dichalcogenides, molybdenum diselenide, PN-junctions, photovoltaic effect, fill factor



The photovoltaic effect (PE), or the creation of a voltage, or an electrical current, in a given material or a solution upon light exposure, was discovered by Becquerel<sup>1</sup> in 1839. Nevertheless, the effective energy harvest from sunlight only became possible in the 1950s with the advent of the silicon PN-junctions.<sup>2</sup> PN-junctions are adjacent hole- and electron-doped semiconducting regions having an interface depleted of charge carriers. PN-junctions are fundamental building blocks for today's electronics and optoelectronics whose fundamental technology is still based on Si despite recent progress in, for example, perovskite solar cells.<sup>3–5</sup>

Several of the transition metal dichalcogenides (TMDs) such as MoS<sub>2</sub>, WSe<sub>2</sub>, and so forth, are semiconducting, but van der Waals bonded solids which are exfoliable down to a single atomic layer.<sup>6,7</sup> These compounds, and their heterostructures, can be grown in high quality and in wafer size area.<sup>8,9</sup> Monolayers display unique optical<sup>10–12</sup> as well as optoelectronic properties<sup>13,14</sup> owing to their direct band gap.<sup>10</sup> It was recently shown<sup>15–20</sup> that it is possible to observe current rectification and the photovoltaic effect in photodiodes electrostatically built through two lateral back-gates to form a horizontal or lateral PN-junctions from a monolayer,<sup>17–19</sup> or from heterostructures composed of atomically thin TMDs in

combination with graphene.<sup>15,16,20,21</sup> In contrast to Si, thin layers of TMDs are inherently flexible, semitransparent, and lack interfacial dangling bonds which, as argued in ref 20 would allow the creation of high-quality heterointerfaces without the constraint of atomically precise commensurability. The availability of TMDs with distinct band gaps<sup>7,22</sup> and work functions opens the possibility of (i) engineering the band gaps in heterostructures and (ii) fabricating translucent photovoltaic tandem cells composed of TMDs having distinct gaps therefore absorbing photons with energies ranging from the ultraviolet (e.g., HfS<sub>2</sub>) to the infrared (e.g., WSe<sub>2</sub>, MoSe<sub>2</sub>, or MoTe<sub>2</sub>).

For horizontal PN-junctions based on a single atomic layer of WSe<sub>2</sub> under white light illumination, ref 17 reports maximum short-circuit current densities  $j_{sc} \sim 0.23$  A/cm<sup>2</sup> (defined as the photogenerated current in the absence of a bias voltage flowing from the junction toward the electrical contacts) for an illumination power density  $p = 1.4 \times 10^3$  W/m<sup>2</sup>. Despite this anomalously large  $j_{sc}$  value, this junction yields a quite modest

Received: August 14, 2015

Revised: October 19, 2015

Published: October 29, 2015

photovoltaic efficiency  $\eta = 0.5\%$ . In turn, ref 13 reports  $j_{sc} \cong 150 \text{ A/cm}^2$  under a fairly large power density  $p \cong 3.2 \times 10^6 \text{ W/m}^2$  yielding a number of photogenerated carriers circulating through the photodetector per adsorbed photon and per unit time, or external quantum efficiency (EQE), of just  $\sim 10^{-3}$ . Small EQEs would suggest rather small power conversion efficiencies.

For vertical heterojunctions composed of single atomic layers of  $\text{MoS}_2$  ( $n$ -doped) and  $\text{WSe}_2$  (either  $p$ -doped or ambipolar), ref 20 reports  $j_{sc}$  values approaching  $1 \text{ mA/cm}^2$  under  $p = 10^6 \text{ W/m}^2$  (laser light with  $\lambda = 532 \text{ nm}$ ). Reference 21, on the other hand, reports  $j_{sc} \cong 13 \text{ mA/cm}^2$  under white light illumination but with a concomitant small  $\eta$  of 0.2%. For multilayered stacks of  $\text{MoS}_2$  and  $\text{WSe}_2$  contacted with graphene, ref 20 reports an incredibly high  $j_{sc}$  value of  $\sim 2.2 \text{ A/cm}^2$  acquired under laser light ( $\lambda = 532 \text{ nm}$ ) and very high power densities. Even larger  $j_{sc}$  values were reported for heterostructures composed of graphene acting as electrodes, and multilayered  $\text{MoS}_2$ ,<sup>16</sup> under laser light with extremely large  $p$ 's ( $>10^6 \text{ W/m}^2$ ). These observations suggest that junctions composed of multilayered TMDs can yield higher photovoltaic currents than monolayers, leading perhaps to higher power conversion efficiencies. Thicker crystals would allow longer photon travel distances within the material thus increasing the probability of generating electron–hole pair(s).

To evaluate this hypothesis, we fabricated lateral PN-junctions (see Figure 1, as well as Methods) based on exfoliated  $h$ -BN (with thicknesses  $t$  ranging between  $\sim 20$  and  $\sim 40 \text{ nm}$ ) on top of which we transferred<sup>23</sup> chemical vapor

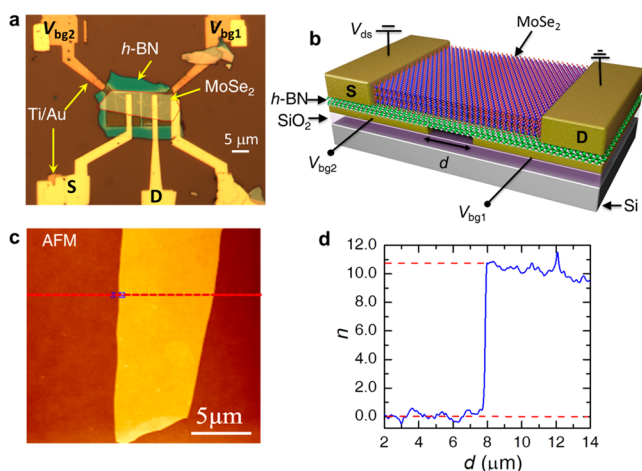


**Figure 1.** (a) Micrograph of a multilayered  $\text{MoSe}_2$  crystal stacked onto a  $\sim 45 \text{ nm}$  thick  $h$ -BN crystal (sample #1), itself placed on a double gate structure patterned on a  $\text{SiO}_2/p$ -Si substrate. A thin red dotted line is used to delineate the  $\text{MoSe}_2$  crystal. The channel length (in between both voltage leads and at either side of the junction) is  $l = 5.52 \mu\text{m}$  and its average width  $w = 6.85 \mu\text{m}$ . The gap between gates is  $\cong 400 \text{ nm}$ . (b) Sketch of a typical sample, indicating the configuration of measurements, e.g., drain (D) and source (S) contacts, excitation voltage  $V_{ds}$ , as well as the voltages applied to the back-gates,  $V_{bg1}$  and  $V_{bg2}$ , respectively. Contacts and gates are composed of  $50 \text{ nm}$  of Au deposited onto a  $5 \text{ nm}$  thick layer of Ti. (c) Atomic force microscopy (AFM) image of the  $\text{MoSe}_2$  crystal on  $\text{SiO}_2$ . The red line depicts the line along which the height profile shown in d was collected. (d) Height profile for the mechanically exfoliated  $\text{MoSe}_2$  crystal showing the number of layers  $n = h/c'$ , where  $h$  is the height of the flake and  $c' = c/2 = 6.4655 \text{ \AA}$  is the interlayer separation ( $c$  is the lattice constant along the interplanar direction<sup>32</sup>).

transport synthesized  $\text{MoSe}_2$  single-crystals, previously found by us to display ambipolar behavior.<sup>24</sup> Although a similar architecture was already reported,<sup>17–19</sup> here we (i) evaluate the properties of a different compound, i.e.,  $\text{MoSe}_2$ , and (ii) evaluate the potential of TMDs for photovoltaic applications by focusing on bulkier crystals. We find that our photodiode is found to exhibit photovoltaic power conversion efficiencies surpassing 14% under standard AM-1.5 solar spectrum. This value is not far from those extracted from the best Si solar cells,<sup>25</sup> i.e., 25%, and compare favorably with those of transparent photovoltaic cells.<sup>26–28</sup> This efficiency is likely to increase, for example, by varying the band gap when tuning the composition, by changing the materials used for the contacts,<sup>15,16</sup> the incorporation or plasmonic nanoparticles,<sup>29</sup> or the optimization of the number of atomic layers. Given their relative transparency in the visible region,<sup>30</sup> and the ability to grow large areas,<sup>8,9,31</sup> we argue that few layer transition metal dichalcogenides present a remarkable potential for photovoltaic applications.

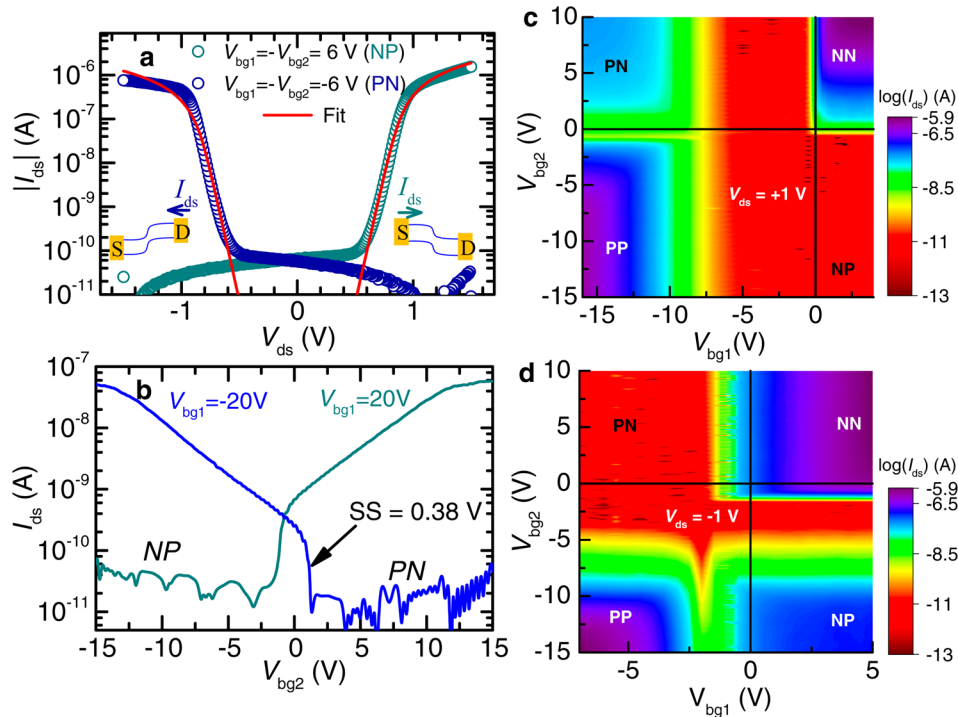
Figure 1a shows a photomicrograph of one of our  $\text{MoSe}_2$  crystals stacked on  $h$ -BN in a lateral PN-junction configuration. Micrographs of additional samples measured for this study are shown in the Supporting Information. As seen, the  $\text{MoSe}_2$  crystal is perceptible but is transparent enough to allow the visualization of both back gates through the  $h$ -BN crystal whose thickness was determined to be  $\sim 45 \text{ nm}$  through atomic force microscopy (AFM). Figure 1b shows a schematic of the measurements, where three independent voltages are applied to the sample, respectively,  $V_{bg1}$  for the left back-gate,  $V_{bg2}$  for the right one, and the bias voltage  $V_{ds}$  through the source and drain contacts. One measures the resulting drain to source current  $I_{ds}$  under or without illumination. Figure 1c shows an AFM image of the  $\text{MoSe}_2$  crystal. The red line indicates the line along which the height profile shown in Figure 1d was collected, which divided by an interlayer spacing<sup>32</sup> of  $6.4655 \text{ \AA}$  indicates a crystal composed of 10–11 atomic layers.

Figure 2a displays the absolute value of the drain to source current  $|I_{ds}|$  for a second multilayered  $\text{MoSe}_2$  or sample #2 ( $8.8 \mu\text{m}$  wide and  $\sim 13$  atomic layers thick) as a function of the excitation voltage  $V_{ds}$ , when 6 V is applied to either gates but with opposite polarity. As expected for a PN-junction, and as previously reported for single-layer  $\text{WSe}_2$  heterostructures,<sup>17–19</sup> our multilayered  $\text{MoSe}_2$  heterostructure displays rectification, or a diode-like response with the sense of current rectification being dependent upon the gate-voltage profile across the junction. Red lines are fits of the observed diode response to the Shockley equation in the presence of a series resistor:<sup>33</sup>

$$I_{ds} = \frac{fV_T}{R_s} W_0 \left( \frac{I_0 R_s}{fV_T} \exp \left( \frac{V + I_0 R_s}{fV_T} \right) \right) - I_0 \quad (1)$$

where  $W$  is the Lambert function and  $V_T$  the thermal voltage, yielding an ideality factor  $f$  of 1.4 with values for the series resistance  $R_s$  ranging from  $0.25$  to  $\sim 0.5 \text{ M}\Omega$ . These  $f$  values are smaller than those in refs 17 and 18 ( $1.9 \leq f \leq 2.6$ ) for single layered  $\text{WSe}_2$  lateral diodes, suggesting a diode response that is closer to the ideal one. The Shockley–Read–Hall recombination theory,<sup>34,35</sup> which assumes recombination via isolated point defect levels, predicts  $f \leq 2$ .

Figure 2b displays  $I_{ds}$  as a function of the gate voltage  $V_{bg2}$  while  $V_{bg1}$  is maintained at a fixed value of  $+20 \text{ V}$  (dark cyan trace) and  $-20 \text{ V}$  (blue trace), respectively. As seen, a sizable drain to source current is observed only when both gate



**Figure 2.** (a) Absolute value of the drain-to-source current  $|I_{ds}|$  on a log–log scale and as a function of the excitation voltage  $V_{ds}$  for two configurations of the back-gate voltages, i.e.,  $V_{bg1} = -V_{bg2} = 6$  V which corresponds to the accumulation of electrons (N) and holes (P) at the respective interfaces, or NP configuration (dark cyan markers), and  $-V_{bg1} = V_{bg2} = 6$  V or PN configuration (blue markers), respectively. Notice the diode-like response as a function of either positive or negative values of  $V_{ds}$ , depending on the sign of the gate voltage(s). Notice the factor of  $10^5$ – $10^6$  increase in current. Red lines are fits to the Shockley diode equation including a series resistance  $R_s$ . For the  $V_{ds} < 0$  V branch one extracts an ideality factor  $f = 1.4$  with  $R_s = 0.45$  M $\Omega$ . For the  $V_{ds} > 0$  V, we obtain  $f = 1.4$  with  $R_s = 0.28$  M $\Omega$ . This data was collected on sample #2 (13 atomic layers). (b) Field-effect characteristics (from sample #1) obtained by keeping the excitation voltage  $V_{ds}$ , and one of the gate-voltages  $V_{bg1}$  at constant values of 0.3 and 20 V, respectively, and by sweeping the second gate-voltage  $V_{bg2}$ . As clearly seen, the field-effect response is ambipolar; i.e., one can accumulate either electrons (for positive values for both gate-voltages) or holes (e.g., negative values for both gate-voltages) in the channel. (c) Contour plot of the logarithm of  $|I_{ds}|$  as a function of both gate voltages and for an excitation voltage  $V_{ds} = +1$  V. These data were collected from sample #1. Notice the clear ambipolar response when both gate voltages have the same polarity or, the rectification-like response when they have opposite polarities. (d) Same as in c but for  $V_{ds} = -1$  V. By comparing c and d, one observes a clear asymmetry in the NP response with respect to the PN one, due to the gate-voltage induced diode response.

voltages have the same polarity, due to the electric-field induced accumulation of charge carriers (transistor operation). The so-called subthreshold swing, or  $SS \sim 380$  mV per decade, is considerably sharper than those values previously observed by us<sup>24</sup> for MoSe<sub>2</sub> on SiO<sub>2</sub>. The same observation applies to the threshold gate voltage for conduction, i.e., the voltage beyond which one extracts a sizable current, which is nearly 1 order of magnitude smaller for *h*-BN substrates, or between 1 and 2 V. Not surprisingly, both observations indicate that *h*-BN is a superior substrate, i.e., less disordered, when compared to SiO<sub>2</sub>.

Finally, Figure 2c and d display contour plots of the logarithm of the drain to source current  $I_{ds}$  as a function of both gate voltages, and for excitation voltages  $V_{ds} = +1$  V and  $-1$  V, respectively. This data set was collected from the sample #1. Currents ranging between  $10^{-12}$  and  $10^{-11}$  A, which correspond to our noise floor, are depicted by the red regions in both plots. Currents ranging from  $\sim 0.1$  to 1  $\mu$ A are depicted by the clear and darker-blue regions, respectively. It is clear that a sizable current is obtained when both gates are simultaneously energized with the same voltage due to the field-effect induced accumulation of charges in the channel. However, both figures become asymmetric when the gates are energized with opposite polarities: sizable currents are observed in the first and in third quadrants of Figure 2c and d, respectively. As expected for PN-junctions, this indicates current rectification but whose diode

response is controllable by the relative polarity between both gate voltages. Having established a well-defined diode response, we proceed with the characterization of their photovoltaic response.

As seen in the Supplementary Figure S3, we evaluated the intrinsic photovoltaic power conversion efficiency of our MoSe<sub>2</sub> crystals (i.e., in absence of back gate-voltage(s)) and under laser illumination ( $\lambda = 532$  nm, spot diameter  $\cong 3.5$   $\mu$ m) finding that it is remarkably small  $\sim 10^{-3}$  %. As explained in the Supporting Information this contrasts markedly with the power conversion efficiencies obtained when both gates are energized to generate the PN-junction. Supplementary Figures S4 and S5 display a thorough characterization of our PN-junctions under laser illumination. We observe very high power conversion efficiencies, i.e.,  $\eta = P_{max}^{el}/P_i \approx 40\%$ , for incident illumination power densities approaching  $p_i = 1000$  W/m<sup>2</sup>, where  $P_{max}^{el}$  corresponds to the maximum photogenerated electrical power. Here, to calculate the incident power  $P_i$ , and similarly to ref 17, we multiplied  $p_i$  by the active area of the junction, or  $A_j = w_c w_j$ , where  $w_c$  is the width of the crystal and  $w_j$  is the gap between both back-gates or the region between gates which is depleted from charge carriers. Although, based on Figure 1a, one could argue that the channel and related PN-junction, might extend well beyond the gap between gates, through nearly the entire channel. Hence, the active area  $A_j$  might end up being

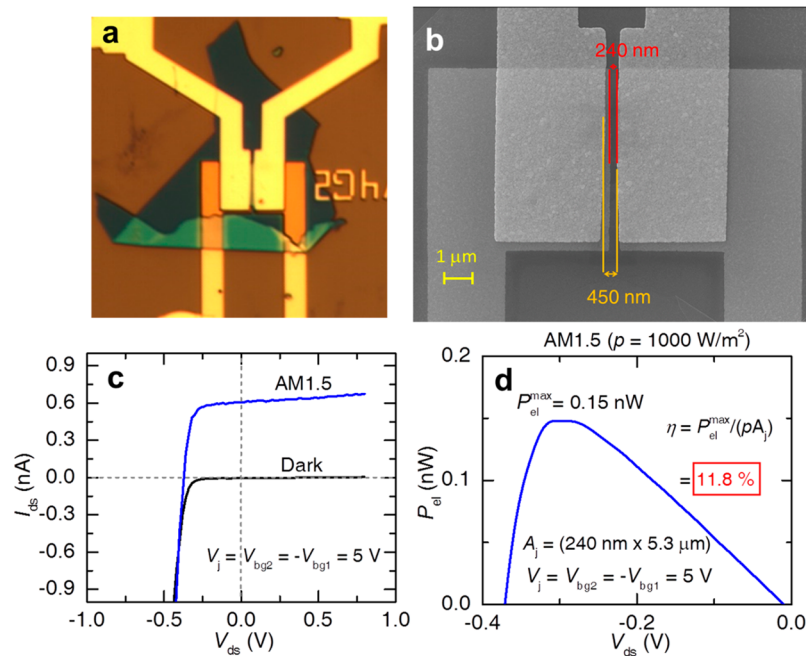


**Figure 3.** (a) Optical micrograph of sample #3. (b) Scanning electron microscopy image indicating the width  $w_j = 240$  nm of the depletion junction and the separation  $l = 450$  nm between drain and source contacts. (c) Drain to source current  $I_{ds}$  as a function of the bias voltage  $V_{ds}$ , when  $V_{bg} = +5$  V is applied to one of the gates and  $V_{bg} = -5$  V is applied to the other. The response in absence of illumination, or under dark conditions, is depicted by the black line while the response under AM 1.5 spectrum is depicted by the blue line. (d) Photogenerated power  $P_{el} = I_{ds} \times V_{ds}$  as a function of  $V_{ds}$  yielding a maximum value of 0.15 nW. When normalized by the illumination power shone onto the junction, i.e.,  $1000 \text{ W/m}^2 \times (240 \times 10^{-9} \times 5.3 \times 10^{-6}) \text{ m}^2$ , one obtains a power conversion efficiency  $\eta = 11.8\%$ . If instead, one used the channel length  $l = 450$  nm, one would obtain  $\eta = 6.3\%$ .

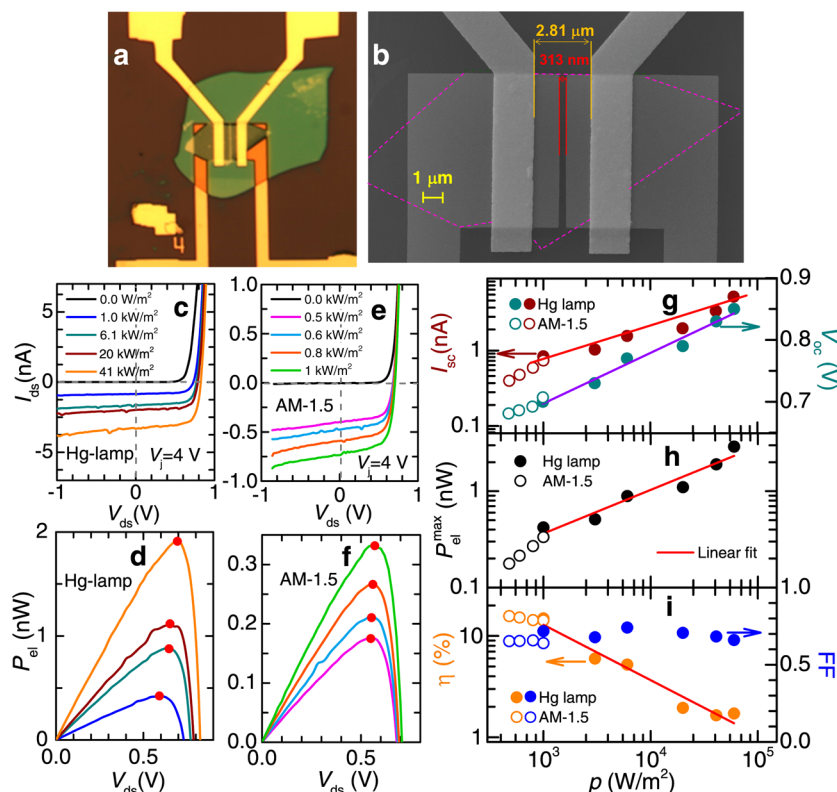
considerably larger than the values calculated by us, and thus necessarily yielding smaller  $\eta$  values. Here, and as shown below, we address this issue by producing PN-junctions whose top metallic contacts cover nearly the entire channel area although still allowing us to illuminate the area of the depleted junction. In addition, we will focus on the evaluation of the photovoltaic power conversion efficiency under the standard Air Mass 1.5 (AM1.5) spectrum which, in contrast to laser illumination, is meaningful from a technological perspective.

Figure 3a shows an optical micrograph of a FET whose channel area is covered by wide drain and source electrical contacts, with the intention of extracting the intrinsic photovoltaic response of the depleted junction.

Given the limited precision of our e-beam lithography system, in Figure 3b we show a scanning electron microscopy image of the same FET, indicating both the final separation  $w_j = 240$  nm between the back gates and the average separation, i.e.,  $d = 450$  nm, between both top electrodes. Figure 3c shows a comparison between the diode-response extracted from this sample, both under AM1.5 (blue line) and in absence of illumination (black trace), when each gate is energized under a constant value of 5 V but of opposite polarity. As seen, under AM1.5 illumination power density ( $1000 \text{ W/m}^2$ ), one extracts a short-circuit current  $I_{sc} = 606 \text{ pA}$  ( $0.1143 \text{ nA}/\mu\text{m}$ ), which contrasts markedly with the values obtained for  $V_{ds} > 0$  V under dark conditions (i.e., oscillating between 1 and 5 pA, and corresponding to our noise floor). Figure 3d, on the other hand, shows the photogenerated electrical power  $P_{el} = I_{ds} V_{ds}$  as a function of  $V_{ds}$ . This curve is obtained by subtracting the black trace from the blue one, which subtracts from the calculated electrical power the contribution from the source-meter. As seen, it peaks at a maximum value  $P_{el}^{\text{max}} = 0.15 \text{ nW}$  which yields a conversion efficiency  $\eta \cong 11.8\%$ , when

renormalized by the illumination power  $P_i = p_i A_j = 1000 \text{ W/m}^2 \times (A_j = 240 \text{ nm} \times w_c = 5.3 \mu\text{m})$  shining on the surface  $A_j$  of the depleted junction. If instead, one used the power applied to the entire channel one would obtain  $\eta \cong 6.3\%$ . This value is 12.6 times larger than  $\eta = 0.5\%$  reported for a lateral PN-junction based on a WSe<sub>2</sub> monolayer,<sup>17</sup> also larger than the value  $\eta = 5.3\%$  reported for MoS<sub>2</sub> monolayers composing a type-II heterojunction with *p*-Si,<sup>36</sup> or larger than  $\eta = 2.8\%$  obtained from plasma doped<sup>37</sup> MoS<sub>2</sub>. For this sample one obtains an open circuit voltage  $V_{oc} = V(I_{ds} = 0 \text{ A}) = 0.364 \text{ V}$  yielding a fill factor  $\text{FF} = P_{el}^{\text{max}} / (I_{sc} V_{oc}) = 0.68$  which is comparable to the values obtained for conventional Si based solar cells.

Metallic surface plasmon polaritons are known to dramatically enhance the interaction between carriers and light in small structures such as sample #3, which have a separation between metallic electrodes comparable to, or smaller than the characteristic wavelength of light.<sup>29,38</sup> Surface plasmon polaritons (SPPs) can propagate back and forth between the metal terminations, effectively creating a Fabry-Perot resonator.<sup>38</sup> This effect could lead to considerably higher photovoltaic power conversion efficiencies,<sup>29</sup> thus contributing to the high efficiencies observed by us. In order to quantify the role of SSPs and their contribution to the above quoted efficiency, we have performed numerical simulations of the light transmission process, to evaluate how much of the incident light is transmitted to the active area defined by the MoSe<sub>2</sub> layer, which is associated with the photovoltaic response of our devices. By using COMSOL Multiphysics, a commercially available solver of Maxwell equations, we were able to calculate the transmission spectra for both *p* (along the channel length) and *s* (polarization perpendicular to the channel length) polarized light, evaluated at the different interfaces of our



**Figure 4.** (a) Optical micrograph of sample #5 which is characterized by a larger separation  $l$  between contacts. (b) Scanning electron microscopy image indicating the width of the depletion junction or  $w_j = 313$  nm, as well as  $l = 2.81$   $\mu\text{m}$ . (c) Drain to source current  $I_{\text{ds}}$  as a function of bias voltage  $V_{\text{ds}}$  under several illumination power densities  $p$ , under the spectrum of a Hg-lamp, and for a multilayered MoSe<sub>2</sub> based PN-junction (sample #4). (d) From the curves in c concomitant photogenerated electrical power  $P_{\text{el}} = I_{\text{ds}}V_{\text{ds}}$  as a function of  $V_{\text{ds}}$ . Here, and for each curve,  $P_{\text{el}}$  was calculated by subtracting the  $p = 0.0$  W/m<sup>2</sup> data (black line). Red markers indicate the maximum photogenerated electrical power values  $P_{\text{el}}^{\text{max}}$ . (e)  $I_{\text{ds}}$  as a function of  $V_{\text{ds}}$  under AM-1.5 spectrum and also for lower  $p$  values using the same setup. (f)  $P_{\text{el}}$  as a function of  $V_{\text{ds}}$ , from the curves in c and calculated in a similar manner. (g) Log–log plot of the short circuit current  $I_{\text{sc}}$  (brown markers) and semilog plot of the open circuit voltage  $V_{\text{oc}}$  (cyan markers) as functions of  $p$ . Red line is a linear fit of  $I_{\text{sc}}(p)$  while the violet line corresponds to a semilogarithmic fit of  $V_{\text{oc}}(p)$ . (h)  $P_{\text{el}}^{\text{max}}$  as a function of  $p$ , from the red markers in d and f. Red line is a linear fit. (i) Photovoltaic efficiency  $\eta$  (orange markers) and fill factor FF (blue markers) as functions of  $p$ . For panels g, h, and i solid and open markers indicate values measured under an Hg lamp and under AM-1.5 irradiation, respectively.

samples. The details concerning our numerical calculations are presented in the [Supporting Information](#). The main outcome of these simulations is that only about 70% of the incident light is impinging at the gap between both back gates acting on the MoSe<sub>2</sub> depleted junction. In other words, for the geometry of our sample, we find that SPPs would be detrimental for its photovoltaic conversion efficiency. Our simulations imply that the actual illumination power density irradiated onto the depleted area is  $\sim 720$  W/m<sup>2</sup> leading to a power conversion efficiency  $\eta \cong 16.4\%$ .

In order to confirm the correct value of  $\eta$ , we also evaluated samples having geometries which are similar to that of sample #1 (see [Figure 1a](#)) but with shorter channel lengths. By varying the length of the channel one should be able to determine if the effective area of the junction extends beyond the depletion area between both gates or, if the only relevant factor when evaluating  $\eta$  is truly the depleted area. Here, we evaluated two samples, having similar crystal widths of  $w_c = 7.5$   $\mu\text{m}$  but distinct thicknesses; sample #4 (12 atomic layers) and characterized under the white light spectrum produced by a Hg lamp and sample #5 (8 atomic layers) characterized under AM1.5.

In [Figure 4a](#), we show an optical image of sample #5, while [Figure 4b](#) shows its scanning electron microscopy image, from

which we extract the precise dimensions of its depleted area, i.e.,  $w_j = 313$  nm, and a crystal width  $w_c = 7.5$   $\mu\text{m}$ . Both samples were previously characterized under coherent  $\lambda = 532$  nm laser light, yielding very similar  $\eta$  values with respect to the ones extracted from samples #1 and #2. Again, to evaluate  $\eta$  we used the dimensions of the carrier depleted area and not the length of the channel which would yield dissimilar  $\eta$  values. This will be illustrated below through a comparison between photovoltaic efficiencies extracted under AM1.5 from samples #3 and #5.

[Figure 4c](#) presents the photodiode response observed from sample #4 under the spectrum of an Hg lamp, namely,  $I_{\text{ds}}$  as a function of  $V_{\text{ds}}$  when the back gates are energized under  $V_j = V_{\text{bg}} = \pm 4$  V. With the Hg lamp one can precisely vary  $p_i$  from 0 to 60 kW/m<sup>2</sup>. Under  $p_i = 1000$  W/m<sup>2</sup>, one extracts  $I_{\text{sc}} = 836$  pA or 0.1115 nA/ $\mu\text{m}$  which is just  $\sim 2.5\%$  smaller than the short circuit current extracted from sample #3 under AM1.5 and  $V_{\text{bg}} = \pm 5$  V. This indicates that an increase in the separation between the electrical contacts by a factor  $>6$  did not lead to any substantial decrease in the photogenerated electrical current due to electron–hole recombination. [Figure 4d](#) displays the photogenerated electrical power  $P_{\text{el}}$  extracted from the traces in [Figure 4c](#) and as a function of  $V_{\text{ds}}$ . As before, to evaluate  $P_{\text{el}}(V_{\text{ds}}, p)$ , we subtracted  $P_{\text{el}}(V_{\text{ds}}, p = 0.0$  W/m<sup>2</sup>),

which should eliminate any spurious contribution from the power supply.

Under  $p_i = 1000 \text{ W/m}^2$  one obtains  $P_{\text{el}}^{\text{max}} = 0.42 \text{ nW}$  which once renormalized by  $P_i = 1000 \text{ W/m}^2 \times (A_j = 7.5 \mu\text{m} \times 400 \text{ nm}) = 2.3475 \text{ nW}$  yields  $\eta = 14.01\%$ . Notice that the typical values for the leakage current flowing through the gates is  $<10^{-11} \text{ A}$ . Hence, when multiplied by  $V_j = 4 \text{ V}$ , one would obtain  $P_{\text{bg}} \cong 0.04 \text{ nW}$  ( $\ll P_{\text{el}}^{\text{max}}$ ) which would correspond to the maximum power applied to the back-gates. The evaluation of the photovoltaic response of sample #5 under AM1.5 is presented in Figure 4e and f which present  $I_{\text{ds}}$  and  $P_{\text{el}}$  as functions of  $V_{\text{ds}}$ , respectively. Under AM 1.5 ( $p_i = 1000 \text{ W/m}^2$ ), one extracts  $I_{\text{sc}} = 738 \text{ pW}$  (or  $0.098 \text{ nA}/\mu\text{m}$ ) and a  $P_{\text{el}}^{\text{max}} = 0.334 \text{ nW}$ . When using  $A_j$  to calculate  $P_i$  one obtains  $\eta = 14.23\%$  which is very close to  $\eta = 14.01\%$  obtained from sample #4 and to  $\eta = 11.8\%$  (or  $16.4\%$  as the simulations imply) extracted from sample #3. Hence all three samples yield consistent  $\eta$  values under white light illumination.

Instead, if one used the area of the channel (between the electrodes) to calculate the  $P_i$  illuminating sample #5, one would obtain  $\eta = 1.58\%$ . This value is 4 times smaller than  $\eta = 6.3\%$  calculated for sample #3 in a similar way. Given that (i) their short circuit currents (in  $\text{nA}/\mu\text{m}$ ) differ by only  $\sim 15\%$  which implies a similar density of photogenerated electron–hole pairs, (ii) that  $P_{\text{el}}^{\text{max}}$  for sample #5 is 2.2 times larger than the value extracted from sample #3, (iii) and that sample #3 exposes a much smaller area of the active material, it would be unphysical to obtain a 4 times higher power conversion efficiency for this sample. Therefore, we conclude that the correct calculation of  $\eta$  ought to be based on the active area of the carrier depleted junction which yields consistent values ranging between  $\sim 14$  and  $\sim 16\%$ . In any case, we have solidly established  $\eta = 6.3\%$  as the bare minimum power conversion efficiency under AM1.5 for a PN-junction composed solely of a transition metal dichalcogenide as the semiconducting channel material. Although our simulations imply that the actual value is  $\eta \cong 8.75\%$ .

Figure 4g displays  $I_{\text{sc}}$  (brown markers) and the extracted open circuit voltages  $V_{\text{oc}}$  (dark green markers) values extracted under the white light spectrum produced by a Hg lamp (solid markers) and under the AM1.5 spectrum (open symbols). Notice that in either case, under the standard power density of  $\sim 10^3 \text{ W/m}^2$ , one would obtain a short circuit current density of  $j_{\text{sc}} \sim 1 \text{ A/cm}^2$  if one normalized  $I_{\text{sc}}$  by the cross-sectional area of the  $\text{MoSe}_2$  crystal. As for any solar cell, this is the current flowing from the junction toward the electrical contacts. However, our geometry is distinct, with the light laterally impacting the junction. Conventional solar cells are vertical stacks of  $n$ -doped and  $p$ -doped material whose top surface is exposed to light. Hence, our  $j_{\text{sc}}$  values cannot be directly compared with those extracted from conventional solar cells, which oscillate around  $40 \text{ mA/cm}^2$ . Nevertheless, we hope that our observations will stimulate theoretical efforts addressing the significance of such pronounced  $j_{\text{sc}}$  values.

$V_{\text{oc}}$  on the other hand is observed to range from  $\sim 0.7$  to  $\sim 0.85 \text{ V}$  which is comparable to  $V_{\text{oc}} \sim 0.7 \text{ V}$  which is a typical value<sup>25</sup> for high-quality monocrystalline Si solar cells. The red line is a power law fit, i.e.,  $I_{\text{sc}} \propto p^\gamma$  yielding  $\gamma \cong 0.4$ , while the brown line is a logarithmic fit of  $V_{\text{oc}}(p)$ . Figure 4h displays  $P_{\text{el}}^{\text{max}}$  as a function of  $p$ , as obtained from the traces in both Figure 4d (solid markers) and f (open markers) with the red line being a power law fit, yielding again an exponent of  $\cong 0.4$ . Finally, Figure 4g displays the resulting  $\eta = P_{\text{el}}^{\text{max}}/P_i$  and the

concomitant fill factor FF, where  $p_i$  was multiplied by the active area of the depletion junction in order to calculate  $P_i$ .  $\eta$  displays power-law dependence as a function of  $p$ . More importantly, under the standard AM-1.5 spectra ( $p \sim 10^3 \text{ W/m}^2$ ),  $\eta$  would surpass  $\sim 14\%$  which is  $\sim 24$  times larger than the maximum value observed for monolayers<sup>17</sup> and exceeds by 1 order of magnitude values previously reported for bulk transition metal dichalcogenides.<sup>39</sup> As previously discussed, and as shown in the Supporting Information, these  $\eta$  values cannot be attributed to the intrinsic photovoltaic response of  $\text{MoSe}_2$  or to the exposed areas adjacent to the PN-junction, since our studies indicate that these areas would yield negligible or very small contributions to the photovoltaic efficiencies reported here.

In summary, our studies on the intrinsic photovoltaic response of multilayered  $\text{MoSe}_2$  field-effect transistors yield photovoltaic power conversion efficiencies  $\eta$  well below  $1\%$ . These values are in general agreement with previous reports based on bulk<sup>39</sup> and on transition metal dichalcogenides single-atomic layers.<sup>17,40</sup> Nevertheless, when a  $\text{MoSe}_2$  crystal composed of  $\sim 10$  atomic layers is transferred onto a flat  $h$ -BN crystal, itself placed on a pair of lateral back-gates to create an electrostatic PN-junction, one observes photovoltaic efficiencies surpassing  $14\%$  under AM-1.5 spectrum, with concomitant fill factors approaching  $0.7$ . These nonoptimized values compare well with those of current Si technologies and with organic tandem solar cells.<sup>41</sup>

An important aspect requiring immediate theoretical attention is to understand the anomalously large short current densities  $>1 \text{ A/cm}^2$  extracted from the lateral geometry used here, which surpass by far those observed of conventional vertically stacked solar cells.<sup>25</sup>

Finally, the sharp increase in efficiency relative to single atomic layers<sup>17,19</sup> is attributable to the increase in sample thickness. This implies that a systematic study as a function of the number of atomic layers is required to expose the maximum photovoltaic efficiencies extractable from these materials. The current challenge is to translate these efficiencies onto large area, vertically stacked heterostructures. Notice that an indirect gap of  $1.41 \text{ eV}$ <sup>42</sup> for multilayered  $\text{MoSe}_2$  would yield a maximum photovoltaic efficiency of  $\eta \sim 35\%$  (for a single PN-junction) according to the Shockley–Queisser limit.<sup>43</sup> While tandem cells composed of transition metal dichalcogenides having distinct band gaps would not be subjected to this limit. Coupled to our results, this implies a remarkable potential for the use of transition metal dichalcogenides in photovoltaic applications specially if these required flexibility and light transmittance.<sup>30</sup>

## ■ ASSOCIATED CONTENT

### 📄 Supporting Information

The Supporting Information is available free of charge on the ACS Publications website at DOI: 10.1021/acs.nanolett.5b03265.

Methods section, describing sample synthesis, device fabrication, experimental setup, examples of fits to the Schokley diode equation with a series resistance, micrographs of samples #2, characterization of the intrinsic photovoltaic response of a multilayered  $\text{MoSe}_2$  crystal under laser light ( $\lambda = 532 \text{ nm}$ ), and the results of our simulation which evaluates the role of surface plasmon polaritons on the transmission of light toward the depleted junction (PDF)

## ■ AUTHOR INFORMATION

## Corresponding Author

\*E-mail: balicas@magnet.fsu.edu.

## Author Contributions

L.B. conceived the project. D.R. synthesized and characterized the single crystals. S.M. produced the devices. N.P. and S.M. performed electrical transport characterization under illumination with the help of Z.L., J.L., and D.S. Measurements under AM1.5 were performed with the support of O.O. A.I.F.D. and F.J.G.V. performed the numerical simulations in order to evaluate the geometry of our samples and the potential role of surface plasmon polaritons. The manuscript was written through contributions of all authors.

## Notes

The authors declare no competing financial interest.

## ■ ACKNOWLEDGMENTS

We acknowledge Prof. P. Kim and Dr. C.-H. Lee for their guidance on the development of our crystal transfer and stacking technique(s), Prof. K. Hanson for allowing access to the Solar Simulator, and Dr. K. Emery, for the critical reading of this manuscript. This work was supported by the U.S. Army Research Office MURI Grant No. W911NF-11-1-0362. J. L. acknowledges the support by NHMFL UCGP No. 5087. Z.L. and D.S. acknowledge the support by DOE BES Division under grant no. DE-FG02-07ER46451. F.J.G.V. acknowledges support from the European Research Council (ERC-2011-AdG proposal no. 290981) The NHMFL is supported by NSF through NSF-DMR-1157490 and the State of Florida.

## ■ REFERENCES

- (1) Becquerel, E. *Comptes Rendus* **1839**, *9*, 561–567.
- (2) Chapin, D. M.; Fuller, C. S.; Pearson, G. L. *J. Appl. Phys.* **1954**, *25*, 676–677.
- (3) Lee, M. M.; Teuscher, J.; Miyasaka, J.; Murakami, T. N.; Snaith, H. J. *Science* **2012**, *338*, 643–647.
- (4) Grinberg, I.; West, D. V.; Torres, M.; Gou, G. Y.; Stein, D. M.; Wu, L. Y.; Chen, G. N.; Gallo, E. M.; Akbashev, A. R.; Davies, P. K.; Spanier, J. E.; Rappe, A. M. *Nature* **2013**, *503*, 509–512.
- (5) Liu, M.; Johnston, M. B.; Snaith, H. J. *Nature* **2013**, *501*, 395–398.
- (6) Coleman, J. N.; Lotya, M.; O'Neill, A.; Bergin, S. D.; King, P. J.; Khan, U.; Young, K.; Gaucher, A.; De, S.; Smith, R. J.; Shvets, I. V.; Arora, S. K.; Stanton, G.; Kim, H. Y.; Lee, K.; Kim, G. T.; Duesberg, G. S.; Hallam, T.; Boland, J. J.; Wang, J. J.; Donegan, J. F.; Grunlan, J. C.; Moriarty, G.; Shmeliov, A.; Nicholls, R. J.; Perkins, J. M.; Grievson, E. M.; Theuwissen, K.; McComb, D. W.; Nellist, P. D.; Nicolosi, V. *Science* **2011**, *331*, 568–571.
- (7) Chhowalla, M.; Shin, H. S.; Eda, G.; Li, L. J.; Loh, K. P.; Zhang, H. *Nat. Chem.* **2013**, *5*, 263–275.
- (8) Kang, K.; Kang, K.; Xie, S. E.; Huang, L. J.; Han, Y. M.; Huang, P. Y.; Mak, K. F.; Kim, C. J.; Muller, D.; Park, J. *Nature* **2015**, *520*, 656–660.
- (9) Gong, Y. J.; Lin, J. H.; Wang, X. L.; Shi, G.; Lei, S. D.; Lin, Z.; Zou, X. L.; Ye, G. L.; Vajtai, R.; Yakobson, B. I.; Terrones, H.; Terrones, M.; Tay, B. K.; Lou, J.; Pantelides, S. T.; Liu, Z.; Zhou, W.; Ajayan, P. M. *Nat. Mater.* **2014**, *13*, 1135–1142.
- (10) Mak, K. F.; Lee, C.; Hone, J.; Shan, J.; Heinz, T. F. *Phys. Rev. Lett.* **2010**, *105*, 136805.
- (11) Ross, J. S.; Wu, S. F.; Yu, H. Y.; Ghimire, N. J.; Jones, A. M.; Aivazian, G.; Yan, J. Q.; Mandrus, D. G.; Xiao, D.; Yao, W.; Xu, X. D. *Nat. Commun.* **2013**, *4*, 1474.
- (12) Jones, A. M.; Yu, H. Y.; Ghimire, N. J.; Wu, S. F.; Aivazian, G.; Ross, J. S.; Zhao, B.; Yan, J. Q.; Mandrus, D. G.; Xiao, D.; Yao, W.; Xu, X. D. *Nat. Nanotechnol.* **2013**, *8*, 634–638.
- (13) Wang, Q. H.; Kalantar-Zadeh, K.; Kis, A.; Coleman, J. N.; Strano, M. S. *Nat. Nanotechnol.* **2012**, *7*, 699–712.
- (14) Lopez-Sanchez, O.; Lembke, D.; Kayci, M.; Radenovic, A.; Kis, A. *Nat. Nanotechnol.* **2013**, *8*, 497–501.
- (15) Britnell, L.; Ribeiro, R. M.; Eckmann, A.; Jalil, R.; Belle, B. D.; Mishchenko, A.; Kim, Y. J.; Gorbachev, R. V.; Georgiou, T.; Morozov, S. V.; Grigorenko, A. N.; Geim, A. K.; Casiraghi, C.; Castro Neto, A. H.; Novoselov, K. S. *Science* **2013**, *340*, 1311–1314.
- (16) Yu, W. J.; Liu, Y.; Zhou, H. L.; Yin, A. X.; Li, Z.; Huang, Y.; Duan, X. F. *Nat. Nanotechnol.* **2013**, *8*, 952–958.
- (17) Pospischil, A.; Furchi, M. M.; Mueller, T. *Nat. Nanotechnol.* **2014**, *9*, 257–261.
- (18) Baugher, B. W. H.; Churchill, H. O. H.; Yang, Y. F.; Jarillo-Herrero, P. *Nat. Nanotechnol.* **2014**, *9*, 262–267.
- (19) Groenendijk, D. J.; Buscema, M.; Steele, G. A.; de Vasconcelos, S. M.; Bratschitsch, R.; van der Zant, H. S. J.; Castellanos-Gomez, A. *Nano Lett.* **2014**, *14*, 5846–5852.
- (20) Lee, C.-H.; Lee, G. H.; van der Zande, A. M.; Chen, W. C.; Li, Y. L.; Han, M. Y.; Cui, X.; Arefe, G.; Nuckolls, C.; Heinz, T. F.; Guo, J.; Hone, J.; Kim, P. *Nat. Nanotechnol.* **2014**, *9*, 676–681.
- (21) Furchi, M. M.; Pospischil, A.; Libisch, F.; Burgdorfer, J.; Mueller, T. *Nano Lett.* **2014**, *14*, 4785–4791.
- (22) Tonndorf, P.; Schmidt, R.; Bottger, P.; Zhang, X.; Borner, J.; Liebig, A.; Albrecht, M.; Kloc, C.; Gordan, O.; Zahn, D. R. T.; de Vasconcelos, S. M.; Bratschitsch, R. *Opt. Express* **2013**, *21*, 4908–4916.
- (23) Li, H.; Wu, J. M. T.; Huang, X.; Yin, Z. Y.; Liu, J. Q.; Zhang, H. *ACS Nano* **2014**, *8*, 6563–6570.
- (24) Pradhan, N. R.; Rhodes, D.; Feng, S. M.; Xin, Y.; Memaran, S.; Moon, B. H.; Terrones, H.; Terrones, M.; Balicas, L. *ACS Nano* **2014**, *8*, 7923–7929.
- (25) Green, M. A.; Emery, K.; Hishikawa, Y.; Warta, W. *Prog. Photovoltaics* **2010**, *18*, 144–150.
- (26) Lunt, R. R.; Bulovic, V. *Appl. Phys. Lett.* **2011**, *98*, 113305.
- (27) Zhao, Y.; Meek, G. A.; Levine, B. G.; Lunt, R. R. *Adv. Opt. Mater.* **2014**, *2*, 606–611.
- (28) Chen, C.-C.; Dou, L. T.; Zhu, R.; Chung, C. H.; Song, T. B.; Zheng, Y. B.; Hawks, S.; Li, G.; Weiss, P. S.; Yang, Y. *ACS Nano* **2012**, *6*, 7185–7190.
- (29) Atwater, H. A.; Polman, A. *Nat. Mater.* **2010**, *9*, 205–213.
- (30) Yoon, J.; Park, W.; Bae, G. Y.; Kim, Y.; Jang, H. S.; Hyun, Y.; Lim, S. K.; Kahng, Y. H.; Hong, W. K.; Lee, B. H.; Ko, H. C. *Small* **2013**, *19*, 3295–3300.
- (31) Wang, X. L.; Gong, Y. J.; Shi, G.; Chow, W. L.; Keyshar, K.; Ye, G. L.; Vajtai, R.; Lou, J.; Liu, Z.; Ringe, E.; Tay, B. K.; Ajayan, P. M. *ACS Nano* **2014**, *8*, 5125–5131.
- (32) James, P. B.; Lavik, M. T. *Acta Crystallogr.* **1963**, *16*, 1183.
- (33) Banwell, T.; Jayakumar, A. *Electron. Lett.* **2000**, *36*, 291–292.
- (34) Shockley, W.; Read, W. T. *Phys. Rev.* **1952**, *87*, 835–842.
- (35) Hall, R. N. *Phys. Rev.* **1952**, *87*, 387.
- (36) Tsai, M.-L.; Su, S.-H.; Chang, J.-K.; Tsai, D.-S.; Chen, C.-H.; Wu, C.-I.; Li, L.-J.; Chen, L.-J.; He, Jr. H. *ACS Nano* **2014**, *8*, 8317–8322.
- (37) Wi, S.; Kim, H.; Chen, M.; Nam, H.; Guo, L. J.; Meyhofer, E.; Liang, X. *ACS Nano* **2014**, *8*, 5270–5281.
- (38) Schuller, J. A.; Barnard, E. S.; Cai, W.; Jun, Y. C.; White, J. S.; Brongersma, M. I. *Nat. Mater.* **2010**, *9*, 193–204.
- (39) Fortin, E.; Sears, W. M. *J. Phys. Chem. Solids* **1982**, *43*, 881–884.
- (40) Sutar, S.; Agnihotri, P.; Comfort, E.; Taniguchi, T.; Watanabe, K.; Lee, J. U. *Appl. Phys. Lett.* **2014**, *104*, 122104.
- (41) Ameri, T.; Li, N.; Brabec, C. *J. Energy Environ. Sci.* **2013**, *6*, 2390–2413.
- (42) Zhang, Y.; Chang, T. R.; Zhou, B.; Cui, Y. T.; Yan, H.; Liu, Z. K.; Schmitt, F.; Lee, J.; Moore, R.; Chen, Y. L.; Lin, H.; Jeng, H. T.; Mo, S. K.; Hussain, Z.; Bansil, A.; Shen, Z. X. *Nat. Nanotechnol.* **2013**, *9*, 111–115.
- (43) Shockley, W.; Queisser, H. J. *J. Appl. Phys.* **1961**, *32*, 510–519.